Heteroclinic and homoclinic connections in a Kolmogorov-like flow

Balachandra Suri,[1,*] Ravi Kumar Pallantla,[2] Michael F. Schatz,[2] and Roman O. Grigoriev[2]
[1]*IST Austria, 3400 Klosterneuburg, Austria*
[2]*School of Physics, Georgia Institute of Technology, Atlanta, Georgia 30332, USA*

(Received 25 April 2019; published 25 July 2019)

Recent studies suggest that unstable recurrent solutions of the Navier-Stokes equation provide new insights into dynamics of turbulent flows. In this study, we compute an extensive network of dynamical connections between such solutions in a weakly turbulent quasi-two-dimensional Kolmogorov flow that lies in the inversion-symmetric subspace. In particular, we find numerous isolated heteroclinic connections between different types of solutions—equilibria, periodic, and quasiperiodic orbits—as well as continua of connections forming higher-dimensional connecting manifolds. We also compute a homoclinic connection of a periodic orbit and provide strong evidence that the associated homoclinic tangle forms the chaotic repeller that underpins transient turbulence in the symmetric subspace.

DOI: 10.1103/PhysRevE.100.013112

I. INTRODUCTION

Turbulent fluid flows are ubiquitous; they can be found in the atmosphere and the oceans, water and oil pipelines, and even in the human aorta. Despite its great practical relevance, a tractable description of turbulent dynamics has remained elusive. However, recent numerical [1,2] and experimental [3–5] studies have shown that unstable recurrent solutions of the Navier-Stokes equation, which governs fluid flows, may prove pivotal in solving this longstanding problem. Often termed exact coherent states (ECSs), such solutions exist for the same parameters as turbulence but are more amenable to numerical analysis given their simple (e.g., steady or periodic) temporal behavior.

The state space description of turbulence best illustrates the dynamical role of ECSs [6,7]. A turbulent flow in physical space maps to a winding trajectory in state space, with each point on it representing a flow field (see Supplemental Material videos 1–7) [8]. In contrast, ECSs such as steady and time-periodic flows are simpler objects (fixed points, closed loops), as shown in Fig. 1. Being unstable, each ECS is a saddle in state space; trajectories in its unstable manifold are repelled away, while those in the stable manifold converge to the ECS [5,9–11]. Heteroclinic (homoclinic) trajectories—which originate in the unstable manifold of an ECS and terminate in the stable manifold of another (the same) ECS—connect different ECSs and create a chaotic saddle in state space [9,12,13]. Dynamics on ECSs, their stable manifolds, heteroclinics, and homoclinics are asymptotically nonchaotic. In this geometrical picture, turbulence represents a deterministic walk between neighborhoods of different ECSs, guided by the corresponding dynamical connections [5,14], both homoclinic and heteroclinic.

Substantial numerical evidence has emerged for the dynamical relevance of ECSs in recent years, mostly from research on three-dimensional (3D) wall-bounded shear flows, such as plane-Couette [15–18], pipe [14,19–21], and channel flows [22–24]. Direct numerical simulation (DNS) of flows in small, spatially periodic domains [25,26] suggests that turbulence at moderate Reynolds numbers (Re) is organized around unstable solutions such as equilibria (EQ) [7,18,27], traveling waves (TWs) [19–22], periodic orbits (POs) [15,17,28], and relative periodic orbits (RPOs) [29,30]. Here TWs (RPOs) are solutions that correspond to steady (time-periodic) states in a reference frame moving in the direction of a

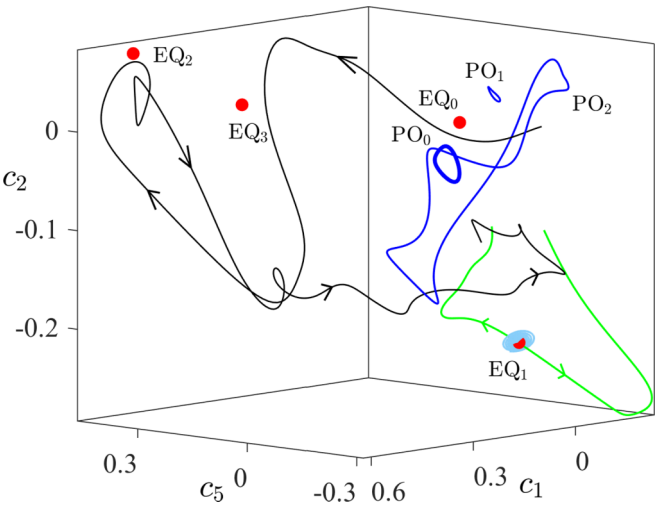

FIG. 1. Low-dimensional projection of the state space generated using data from numerical simulation of a weakly turbulent Kolmogorov-like flow. Instantaneous snapshots of the flow in the physical space are associated with points in the state space. Turbulent evolution is represented by a trajectory (black curve) passing through neighborhoods of unstable equilibria (spheres) and periodic orbits (loops). Stable and unstable manifolds (green curves and light blue surface) of these solutions constrain the dynamics in their neighborhoods. The projection method is described in Appendix A.

*Corresponding author: bsuri@ist.ac.at

continuous symmetry (e.g., along the axis of a pipe). Flow fields resembling ECSs were also observed in a few laboratory experiments [3–5,31], which further validated their relevance in turbulence.

The geometry of chaotic saddle shaped by invariant (stable and unstable) manifolds and dynamical connections between ECSs, however, remains under-explored. In particular, the connectivity of different neighborhoods can be determined by generating a dense set of trajectories spanning the unstable manifold of an ECS and identifying which neighborhoods are subsequently visited by each trajectory [7,14]. However, dynamically relevant ECSs have several (three of more) unstable directions [11,13,14,18,30], which renders this procedure computationally expensive. To circumvent this challenge numerical studies to date have analyzed dynamics confined to invariant subspaces (e.g., symmetry subspaces, laminar-turbulent boundary) which reduces the number of dynamically relevant ECSs as well as the dimensionality of their unstable manifolds. Using this technique, several previous studies [9,14,15,24,28,32] identified trajectories that originate at ECSs with only one or two unstable directions and subsequently approach another ECS. However, such trajectories were not proven to asymptotically converge to an ECS. Hence, they can only be regarded as likely signatures of dynamical connections.

Even within invariant subspaces, very few dynamical connections between ECSs have been found. Gibson *et al.* [7] and Halcrow *et al.* [12] computed four heteroclinic connections between unstable EQs in plane-Couette flow (PCF). Using low-dimensional projections of state space, the authors showed that turbulent trajectories are transiently guided by these connections. The structural stability of these connections—their robustness to small changes in Re—was also discussed using dimension counting arguments [33]. Two homoclinic orbits of a PO in PCF were computed by van Veen *et al.* [34] using a multishooting algorithm [35]. The authors suggested that dynamics along these connections resemble the "bursting" phenomenon observed in turbulent boundary layers [36]. Riols *et al.* [37], in a study of subcritical transition to magnetorotational dynamo in Keplerian shear flows, computed both homoclinic and heteroclinic connections between unstable POs. Pershin *et al.* [38] found a heteroclinic connection from an EQ to a nearby PO in PCF. In both Riols *et al.* and Pershin *et al.*, connections were computed very close to the saddle-node bifurcations leading to the formation of these invariant solutions. Recently, Budanur *et al.* [39] computed a homoclinic orbit of a spatially localized RPO in pipe flow and suggested that the associated homoclinic tangle underlies transient turbulence in this flow. All the connections listed above originate (terminate) at ECSs with only one or two (one or zero) unstable directions, which facilitates the use of simple shooting and bisection algorithms. Recently Farano *et al.* [13] showed that an adjoint-based method can be used to find connections between neighborhoods of unstable EQs in PCF where the originating (destination) EQs has more than two (one) unstable direction.

Despite these advances, an extensive exploration of state space to detect signatures of connections between dynamically dominant ECSs has not been carried out yet. For instance, some previous studies computed connections between ECSs of the same type (i.e., between EQs or between POs) [7,12,34] while others reported only isolated connections between POs and EQs [37,38]. The chaotic saddle, however, is shaped by ECSs of different types and a complex network of dynamical connections between them. To address this shortcoming of previous studies, we report in this article a systematic and exhaustive exploration of low-dimensional unstable manifolds of ECSs to detect dynamical connections between various types on ECSs.

The system we numerically study is the quasi-two-dimensional (Q2D) Kolmogorov-like flow in a shallow electrolyte layer driven by a horizontal, (spatially) near-sinusoidal body force. Q2D flows are computationally more tractable than 3D flows since they can be accurately described using a 2D model [40,41]. In fact, the relative simplicity of DNS of 2D flows has prompted researchers in recent years to carry out the most systematic exploration of ECSs in 2D turbulence [42–44]. For instance, Chandler *et al.* [42] studied 2D Kolmogorov flow on a periodic domain to test whether turbulent statistics can be reproduced using suitable averages over time-periodic solutions [45]. More recently, Suri *et al.* [5,11] have validated the dynamical role of EQs and their unstable manifolds, for the first time in laboratory experiments, using Q2D Kolmogorov-like flow as the test bed. 2D DNS of flow in these studies [5,11] was performed on a numerical domain with lateral dimensions and boundary conditions identical to those in the experiment, facilitating quantitative comparison between theory and experiment.

This article is structured as follows: In Sec. I we discuss the 2D model for Q2D flows and its numerical implementation. In Secs. III A–III D we explore invariant manifolds of various EQs and POs and identify heteroclinic and homoclinic connections. The stability of dynamical connections to small changes in Reynolds number is discussed in Sec. III E. In Sec. III F we discuss the relation between the dynamical connections and transient turbulence. Finally, we summarize our findings and discuss their significance in Sec. IV.

II. QUASI-2D KOLMOGOROV-LIKE FLOW

The evolution of weakly turbulent flows in an electromagnetically driven shallow electrolyte layer is modeled here using a strictly 2D equation [41]

$$\partial_t \mathbf{u} + \beta \mathbf{u} \cdot \boldsymbol{\nabla} \mathbf{u} = -\boldsymbol{\nabla} p + \frac{1}{\mathrm{Re}}(\nabla^2 \mathbf{u} - \gamma \mathbf{u}) + \mathbf{f}, \qquad (1)$$

which is derived by averaging the 3D Navier-Stokes equation in the vertical (z) direction [41]. Here $\boldsymbol{\nabla}$ is the gradient operator restricted to the horizontal dimensions x, y, and $\mathbf{u}(x, y, t)$ is the velocity field at the electrolyte-air interface, which is assumed to be incompressible ($\boldsymbol{\nabla} \cdot \mathbf{u} = 0$). This is an accurate approximation for moderate Reynolds numbers ($\mathrm{Re} \lesssim 40$) [41]. $\mathbf{f}$ is the nondimensionalized depth-averaged horizontal forcing profile, and p plays the role of the 2D kinematic pressure. In Q2D flows, the solid boundary beneath the fluid layer causes a vertical gradient in the magnitude of the horizontal velocity. The prefactor $\beta \neq 1$ and linear friction $-\gamma \mathbf{u}$ model the effective change in inertia and the shear stress, respectively, due to this vertical gradient [40,41]. For the flow in experiments detailed in Suri *et al.* [5], which

we numerically study in this article, $\beta = 0.83$ and $\gamma = 3.22$. We note that these values differ significantly from $\beta = 1$ and $\gamma = 0$ corresponding to an unphysical strictly 2D flow typically studied in numerics [42,44]. The Reynolds number Re describes the strength of electromagnetic forcing and serves as the parameter that controls the complexity of flow. The dimensional form of Eq. (1) and analytical expressions for β, γ, and Re as functions of experimental parameters are provided in Refs. [41] and [46].

DNS of the flow was performed using a finite-difference code previously employed in Refs. [5,11,46]. Velocity and pressure fields on a computational domain with lateral dimensions $(L_x, L_y) = (14, 18)$ were spatially discretized using a 280×360 staggered grid with spacing $\delta x = \delta y = 0.05$ between grid points. No-slip boundary conditions were imposed on the velocity field, and spatial derivatives were approximated using second-order central finite difference formulas. Temporal integration of Eq. (1) was performed using the semi-implicit P2 projection scheme to enforce incompressibility of the velocity field at each time step [47]. The linear (nonlinear) terms in Eq. (1) were discretized in time using the second order implicit Crank-Nicolson (explicit Adams-Bashforth) method. A time step $\delta t \leqslant 1/100$ was used for temporal integration to ensure the CFL number $\max\{u_x\delta t/\delta x, u_y\delta t/\delta y\} \leqslant 0.5$.

In a 2D Kolmogorov flow, the forcing profile is strictly sinusoidal, i.e., $\mathbf{f} \propto \sin(\pi y)\,\hat{\mathbf{x}}$. In experiments detailed in Refs. [5,46], however, the electromagnetic forcing is sinusoidal only near the center of the domain and decays to zero at the boundaries. To replicate this forcing, we used a dipole lattice approximation of the magnet array in the experiment and computed the resulting electromagnetic forcing. Comparison between experimentally measured forcing profile and the numerically estimated one was provided in Tithof *et al.* [46]. The 2D forcing profile $\mathbf{f}$ computed from the dipole lattice model is antisymmetric under the coordinate transformation $\mathcal{I} : (x, y) \to (-x, -y)$, i.e., $\mathcal{I}\mathbf{f} = -\mathbf{f}$. This twofold inversion symmetry ($\mathcal{I}^2 = 1$) is equivalent to rotation by π about the z axis passing through the lateral center of the computational domain. Under $\mathcal{I}$, the velocity field transforms as $\mathcal{I}\mathbf{u}(x, y, t) \to -\mathbf{u}(-x, -y, t)$, which makes Eq. (1) equivariant under $\mathcal{I}$.

A consequence of this equivariance is that the symmetry of a rotationally invariant flow is preserved during its time evolution, i.e., the symmetry subspace $\mathcal{S} = \{\mathbf{u} \in \mathcal{M} \,|\, \mathcal{I}\mathbf{u} = \mathbf{u}\}$ of $\mathcal{M}$ is invariant. Here $\mathcal{M}$ represents the full state space. All ECSs and connections between them we report in this article lie in $\mathcal{S}$. Since trajectories in $\mathcal{S}$ are generally unstable, numerical errors will accumulate such that $\mathbf{u}(t)$ will eventually leave $\mathcal{S}$ even if $\mathbf{u}(0) \in \mathcal{S}$. To prevent this, we augmented the numerical integrator by projecting $\mathbf{u}(t)$ back into $\mathcal{S}$ after every time step [48].

III. RESULTS

As Re is increased, the Kolmogorov-like flow undergoes a number of bifurcations before transitioning to weak turbulence at Re ≈ 18 [46]. At Re ≈ 22 the flow in full state space $\mathcal{M}$ is chaotic, which was confirmed by computing the Lyapunov spectrum of a long turbulent trajectory using continuous Gram-Schmidt orthogonalization [11,49]. In this dynamical regime we previously identified 31 unstable equilibria of the 2D model [11]. Twenty-eight of these were outside of $\mathcal{S}$. Furthermore, their unstable manifolds were relatively high-dimensional in $\mathcal{M}$ (with the number of unstable directions as low as three and as high as twenty) and thus computationally forbidding to map out. Hence, we instead started our analysis with the equilibria in $\mathcal{S}$, labeled EQ_0, EQ_1, and EQ_2.

TABLE I. The number of unstable directions N_u and the leading eigenvalue(s) [Floquet exponent(s)] λ for the recurrent solutions we computed in $\mathcal{S}$ at Re = 22.05.

	N_u		λ	
	$\mathcal{S}$	$\mathcal{M}\backslash\mathcal{S}$	$\mathcal{S}$	$\mathcal{M}\backslash\mathcal{S}$
EQ_0	0	2	$-0.004 \pm 0.020i$	$0.058 \pm 0.047i$
EQ_1	1	2	0.017	0.029
EQ_2	2	5	$0.035 \pm 0.114i$	0.022
EQ_3	1	2	0.068	$0.029 \pm 0.029i$
PO_0	0	3	$-0.003 \pm 0.059i$	0.151
PO_1	1	2	0.036	$0.054 \pm 0.033i$
PO_2	1	3	0.044	0.049
QP_1	1	–	–	–

The stability properties of these equilibria and other recurrent solutions we found in $\mathcal{S}$ are summarized in Table I. We have listed the number of unstable directions N_u and the leading eigenvalues λ for EQs (Floquet exponents for POs) both in the symmetry invariant subspace $\mathcal{S}$ and in the rest of state space, i.e., $\mathcal{M}\backslash\mathcal{S}$. All ECSs we computed have two or fewer unstable directions in $\mathcal{S}$, which allows their unstable manifolds to be well-approximated with a dense set of trajectories [11]. Note that EQ_0 and PO_0 are stable in $\mathcal{S}$. Hence, turbulence in $\mathcal{S}$ can be transient, with trajectories converging to one of these two ECSs asymptotically in time. This is indeed what numerical simulations show, as we discuss in Sec. III F.

Connection(s) from an origin ($ECS_{-\infty}$) to a destination (ECS_{∞}) lie at the intersection of the unstable manifold of $ECS_{-\infty}$ and the stable manifold of ECS_{∞}. Since the dimensionality of stable manifolds is very high ($O(10^5)$ in our case), we will search the low-dimensional unstable manifolds of ECSs for dynamical connections. Such unstable manifolds can be conveniently approximated by families of trajectories $\mathbf{u}(\mathbf{p}, t)$ that start near an ECS, where the unstable manifold is locally tangent to the linear subspace parametrized by the unstable and marginal eigenvectors of that ECS. Here $\mathbf{p}$ parametrizes the family of manifold trajectories. The specifics of constructing a linear subspace, and consequently its parametrization, depend on the type of ECS (EQ or PO) as well as the dimensionality of its unstable manifold, as discussed below.

Table I shows that several solutions we identified have a single unstable direction in $\mathcal{S}$. The unstable manifold of such ECS is naturally divided into two halves, which correspond to the positive and negative halves of the corresponding linear subspace (see Fig. 1). We shall hereafter refer to these halves as $\mathbf{u}^{\pm}(\mathbf{p}, t)$. Furthermore, $\mathbf{u}^{\pm}(\mathbf{p}, t)$ lie on the opposite sides

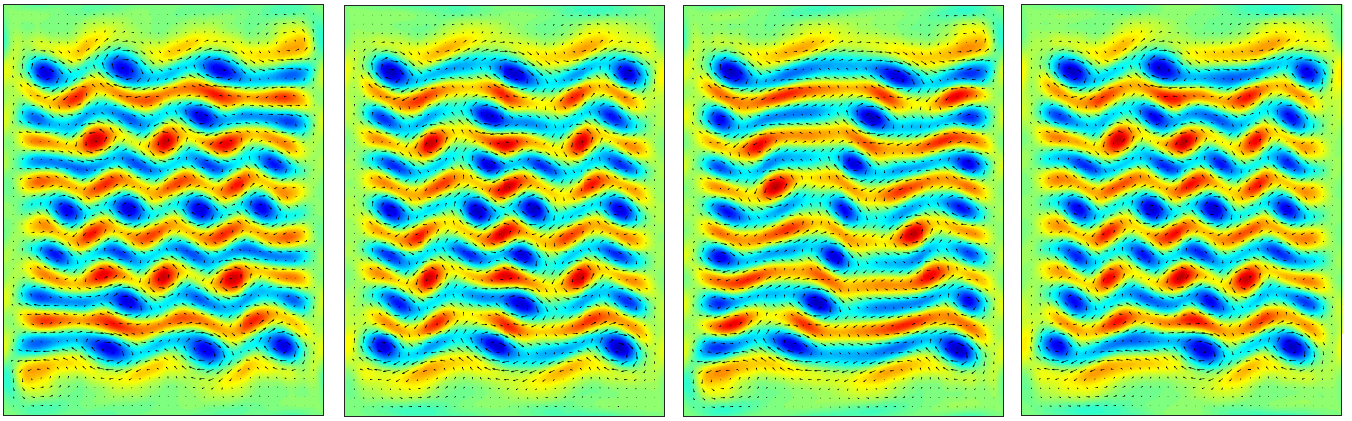

FIG. 2. Rotationally symmetric equilibrium solutions (a) EQ_2, (b) EQ_0, (c) EQ_1, (d) EQ_3. Color (black arrows) indicates vorticity (velocity).

of the stable manifold of the ECS, which serves as a local separatrix and repels trajectories near the ECS along $\mathbf{u}^+(\mathbf{p},t)$ or $\mathbf{u}^-(\mathbf{p},t)$. This allows us to compute connections terminating at ECSs with one unstable direction using a simple bisection method [23]. In the following sections we provide a detailed discussion of connections between various ECSs listed in Table I.

A. Connections originating at EQ_2

We start our analysis with equilibrium EQ_2, which has the highest dimensional unstable manifold of all the EQs in $\mathcal{S}$. The vorticity field ($\omega = \nabla\times\mathbf{u}$) associated with EQ_2 is shown in Fig. 2(a). The 2D unstable manifold of EQ_2 is locally tangent to the plane spanned by the complex conjugate pair of unstable eigenvectors $\hat{\mathbf{e}}_1$, $\hat{\mathbf{e}}_2 = \hat{\mathbf{e}}_1^*$ associated with $\lambda_{1,2} = \sigma \pm i\mu$, where $\sigma = 0.035$ and $\mu = 0.114$. To construct this 2D surface, which lies entirely in $\mathcal{S}$, we generated 360 initial conditions $\mathbf{u}(\theta, 0)$ on a circle around EQ_2 in the plane spanned by $\hat{\mathbf{e}}_1$, $\hat{\mathbf{e}}_2$:

$$\mathbf{u}(\theta,0) = \mathbf{u}_{eq} + \epsilon\cos(\theta)\,\hat{\mathbf{e}}'_1 + \epsilon\sin(\theta)\,\hat{\mathbf{e}}'_2. \tag{2}$$

Here $\mathbf{u}_{eq}$ corresponds to EQ_2 and $\hat{\mathbf{e}}'_1$, $\hat{\mathbf{e}}'_2$ are real orthonormal vectors constructed from the real and imaginary parts of $\hat{\mathbf{e}}_1$, $\hat{\mathbf{e}}_2$. For numerical convenience we chose $\epsilon = 0.002\cdot\|\mathbf{u}_{eq}\|$ and positioned the initial conditions $\mathbf{u}(\theta,0)$ at equal angular intervals $\Delta\theta = 2\pi/360$ on the circle. Numerical integration of initial conditions $\mathbf{u}(\theta,0)$ generates trajectories $\mathbf{u}(\theta,t)$ that approximate the 2D manifold and parametrize it by θ, t. Each manifold trajectory $\mathbf{u}(\theta,t)$ was computed on a temporal interval of length $25\tau_c$, where $\tau_c = 12.5$ (nondimensional time units) is the average temporal autocorrelation time [11].

In the neighborhood of EQ_2, the various trajectories $\mathbf{u}(\theta,t)$ initially evolve spiraling outward:

$$\mathbf{u}(\theta,t) \approx \mathbf{u}_{eq} + \epsilon e^{\sigma t}\cos(\theta+\mu t)\,\hat{\mathbf{e}}'_1 + \epsilon e^{\sigma t}\sin(\theta+\mu t)\,\hat{\mathbf{e}}'_2. \tag{3}$$

To illustrate this, we plotted a portion of the 2D unstable manifold in Fig. 3, projected onto vectors $\hat{\mathbf{e}}'_1$ and $\hat{\mathbf{e}}'_2$. Only one in every ten trajectories generated is shown, and the segment of each trajectory $\mathbf{u}(\theta,t)$ plotted corresponds to $0 \leqslant t \leqslant 11\tau_c$.

Coordinates c_1, c_2 in Fig. 3 are the normalized inner products,

$$c_k(t) = \frac{(\mathbf{u}(\theta,t) - \mathbf{u}_{eq})\cdot\hat{\mathbf{e}}'_k}{D_c}, \tag{4}$$

where $D_c = \max_{t,t'}\|\mathbf{u}(t) - \mathbf{u}(t')\| = 300$ is the empirically estimated maximum separation between two points on an $800\tau_c$-long turbulent trajectory in $\mathcal{S}$, which defines the "diameter" of the chaotic repeller. Normalizing distances with D_c ensures that points separated by nearly unit distance in the low-dimensional projection are very far apart in full state space. Notice that, farther away from EQ_2 ($|c_1|, |c_2| > 0.2$), the shape of $\mathbf{u}(\theta,t)$ becomes fairly complicated due to the nonlinearity of the governing Eq (1).

It is not known *a priori* which $\mathbf{u}(\theta,t)$ approach an ECS (EQ or PO) closely after leaving the neighborhood of EQ_2. Previously, Gibson *et al.* [7] and Halcrow *et al.* [12] inferred possible dynamical connections by inspecting low-dimensional state space projections. In contrast, Riols *et al.* [37] analyzed time series of (magnetic) energy and identified close passes to

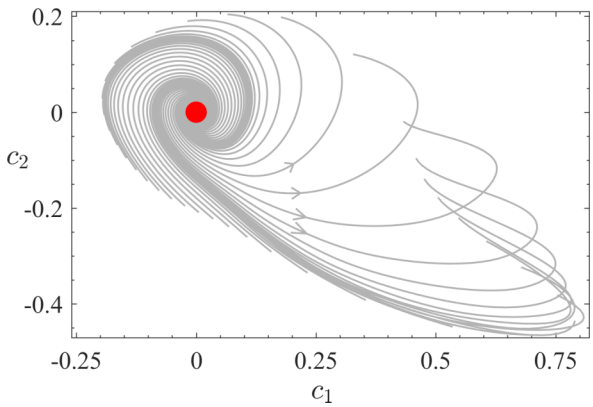

FIG. 3. Trajectories $\mathbf{u}(\theta,t)$ (gray curves) approximating the unstable manifold of EQ_2 (red sphere). $\mathbf{u}(\theta,t)$ originate on a small circle around EQ_2 that lies in a plane spanned by the complex conjugate pair of unstable eigenvectors $\hat{\mathbf{e}}_1$ and $\hat{\mathbf{e}}_2$. Coordinates c_1, c_2 are projections of $\mathbf{u}(\theta,t)$ onto orthonormal vectors constructed from $\hat{\mathbf{e}}_1$, $\hat{\mathbf{e}}_2$.

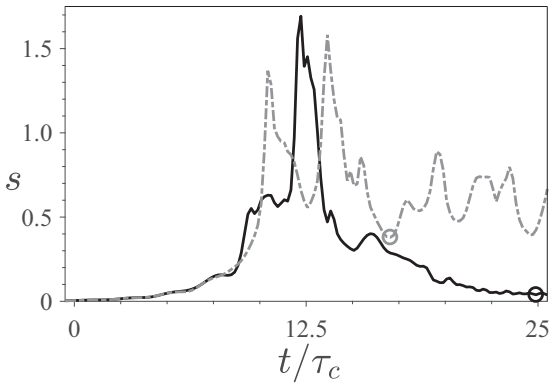

FIG. 4. State space speeds $s(\theta, t)$ along two trajectories in the unstable manifold of EQ_2 that exhibit contrasting dynamics. Solid (dashed) curve is speed along a trajectory that approaches (does not approach) an equilibrium closely after leaving the neighborhood of EQ_2. The lowest speed $s_m(\theta) = \min_t s(\theta, t)$ for $t/\tau_c \in [10, 25]$ for each curve is marked using an open circle.

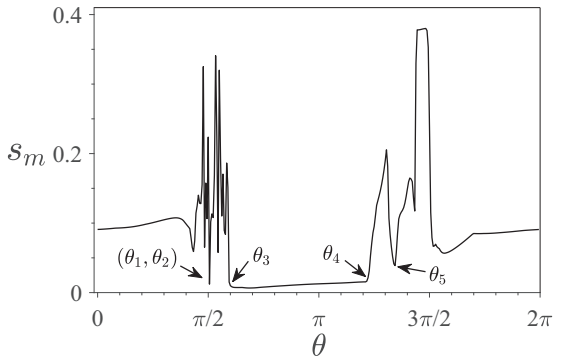

FIG. 5. Minimum state space speed $s_m(\theta) = \min_t s(\theta, t)$ along each trajectory $\mathbf{u}(\theta, t)$ in the 2D unstable manifold of EQ_2. Trajectories corresponding to $s_m \ll 1$ are possible dynamical connections from EQ_2 to an equilibrium.

POs using intervals with "periodic" behavior. Both these techniques, however, require visual inspection and detecting signatures of dynamical connections cannot be automated. In this study we tested two methods to detect signatures of dynamical connections that do not require laborious visual inspection. The method employed for detecting connections that terminate at EQs proved very effective and is discussed next. A method for detecting connections to POs using recurrence analysis [9] is discussed in Appendix B.

For each trajectory $\mathbf{u}(\theta, t)$ in the unstable manifold of EQ_2, we computed the normalized instantaneous state space speed $s(\theta, t)$, which we define as [5,11]

$$s(\theta, t) = \frac{\tau_c}{\|\mathbf{u}(\theta, t)\|} \|\partial_t \mathbf{u}(\theta, t)\|. \tag{5}$$

Since $\partial_t \mathbf{u} = 0$ ($s = 0$) for any EQ, $s(\theta, t) \ll 1$ indicates that a trajectory $\mathbf{u}(\theta, t)$ in state space is near an EQ [5,50]. In the physical space, this corresponds to the evolution of the flow dramatically slowing down. Figure 4 shows, as examples, the speed plots for two different manifold trajectories, $\mathbf{u}(\pi/2, t)$ and $\mathbf{u}(3\pi/2, t)$. Clearly, $\mathbf{u}(\theta, t)$ lie in the linear neighborhood of EQ_2 for $0 < t \lesssim 10\tau_c$ ($s \ll 1$) and $s(\theta, t)$ grows exponentially according to Eq. (3). After this initial transient, however, dynamics described by various trajectories can be qualitatively very different. For instance, the shape of $s(3\pi/2, t)$ (gray curve) suggests that $\mathbf{u}(3\pi/2, t)$ displays turbulent evolution. In contrast, $s(\pi/2, t)$ (black curve) suggests that $\mathbf{u}(\pi/2, t)$ approaches an EQ closely after a brief turbulent excursion. Hence, to test if a trajectory $\mathbf{u}(\theta, t)$ approaches an EQ *after* it departs from the neighborhood of EQ_2, we computed the minimum speed $s_m(\theta) = \min_t s(\theta, t)$ for $10\tau_c \leqslant t \leqslant 25\tau_c$, which is shown in Fig. 5. The low values of $s_m(\theta)$ for $\theta \in (\theta_1, \theta_2)$, $\theta \in (\theta_3, \theta_4)$, and $\theta = \theta_5$ strongly suggest that the corresponding trajectories $\mathbf{u}(\theta, t)$ closely shadow either heteroclinic or homoclinic connections from EQ_2 to other EQs. In Fig. 5 the uncertainty in θ is limited by the angular resolution $\Delta\theta$ in the initial conditions $\mathbf{u}(\theta, 0)$. Consequently, to compute exact dynamical connections, the estimates for θ may require refinement in some cases. The labels θ_1 through θ_5 in Fig. 5 correspond to these refined values. Also, $s_m(\theta) > 0$ even for trajectories $\mathbf{u}(\theta, t)$ that correspond exactly to dynamical connections. This is because minima in the $s(\theta, t)$ are computed on a finite temporal interval, while dynamical connections converge ($s_m = 0$) to the destination EQs only in infinite time.

The destination EQs that different dynamical connections approach were computed using a Newton solver [51–53] initialized with the flow field $\mathbf{u}(\theta, t)$ at the instant when $s(\theta, t) = s_m(\theta)$. For $\theta \in (\theta_1, \theta_2)$ and $\theta \in (\theta_3, \theta_4)$ the solver converged to EQ_0, which is a stable node in $\mathcal{S}$. For $\theta = \theta_5$ the solver converged to EQ_1, which is a saddle with one unstable direction in $\mathcal{S}$. The flow fields corresponding to EQ_0 and EQ_1 are shown in Figs. 2(b) and 2(c). Dimensional arguments (discussed in Sec. III E) suggest that connections from EQ_2 to EQ_0 should comprise a one-parameter family forming a 2D manifold, just like those in the interval (θ_3, θ_4). However, the difference $\theta_2 - \theta_1$ is smaller than the resolution $\Delta\theta$ in case of the interval (θ_1, θ_2). Consequently, θ_1, θ_2 cannot be distinguished in Fig. 5. Hereafter, we will refer to θ in this narrow interval (θ_1, θ_2) collectively as θ_n. The wide interval (θ_3, θ_4) will be referred to as θ_w. To confirm that the dynamical connections originating at EQ_2 indeed terminate at either EQ_0 or EQ_1, we need to make sure that the distance

$$D_0 = \min_t \frac{\|\mathbf{u}(\theta, t) - \mathbf{u}_{eq}\|}{D_c} \tag{6}$$

vanishes in the limit $t \to \infty$. Here $\mathbf{u}_{eq}$ is the velocity field corresponding to the destination EQ. For all connections reported in this study, we chose $D_0 < 0.005$ as the criterion for convergence.

Let us start our analysis with the trajectories $\mathbf{u}(\theta_n, t)$ and $\mathbf{u}(\theta_w, t)$ that approach the equilibrium EQ_0 which is stable in $\mathcal{S}$. The eigenvalues of weakly contracting modes of EQ_0 are $\lambda_{1,2} = -0.004 \pm 0.020i$, $\lambda_{3,4} = -0.012 \pm 0.42i$. Consequently, most nearby trajectories in $\mathcal{S}$ converge to EQ_0 at a rate determined by the real part of λ_1 ($\mathcal{R}\{\lambda_1\}$). Hence, we computed trajectories $\mathbf{u}(\theta_n, t)$ and $\mathbf{u}(\theta_w, t)$ for an interval of duration $350\tau_c \gg 1/\mathcal{R}\{\lambda_1\} \approx 10\tau_c$. At the end of numerical integration both $\mathbf{u}(\theta_n, t)$ and $\mathbf{u}(\theta_w, t)$ approached EQ_0 to within a distance $D_0 < 10^{-8}$, confirming that we have indeed found heteroclinic connections from EQ_2 to EQ_0. Hereafter,

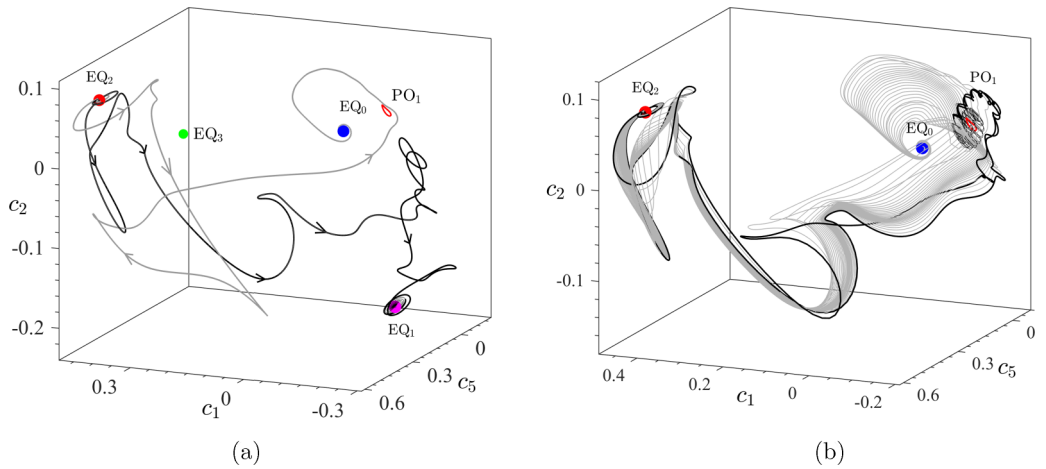

FIG. 6. Heteroclinic connections from EQ_2 to various ECSs. (a) A connection (gray curve) to EQ_0 that belongs to the family DC_1 and an isolated connection DC_3 (black curve) to EQ_1 (b) Family of connections DC_2 (gray curves) that terminate at EQ_0 and isolated connections DC_6, DC_7 (black curves) to PO_1.

we shall refer to these dynamical (heteroclinic) connections corresponding to $\mathbf{u}(\theta_n, t)$ and $\mathbf{u}(\theta_w, t)$ as DC_1 and DC_2, respectively. A connection from the family DC_1 is shown (gray curve) in Fig. 6(a), and 30 connections from DC_2 that are equally spaced on the interval (θ_3, θ_4) are shown in Fig. 6(b). Both figures show the projection of state space onto an orthogonal basis constructed from the stable eigenvectors $\hat{\mathbf{e}}_1$, $\hat{\mathbf{e}}_2$, and $\hat{\mathbf{e}}_5$ of EQ_0. The vectors $\hat{\mathbf{e}}_1$, $\hat{\mathbf{e}}_2$ were chosen to visualize asymptotic dynamics along the connections terminating at EQ_0. The vector $\hat{\mathbf{e}}_5$ was chosen because trajectories $\mathbf{u}(\theta, t)$ far from EQ_0 have large components along this direction. We note that, unless mentioned otherwise, these modes are used for all state space projections in this article.

In Fig. 6 both DC_1 and DC_2 converge to EQ_0 spiraling inwards, almost entirely confined to the c_1-c_2 plane. This is a consequence of the large separation between the real parts of $\lambda_{1,2}$ and $\lambda_{3,4}$, which makes $\hat{\mathbf{e}}_1$, $\hat{\mathbf{e}}_2$ the only dynamically relevant eigenvector pair near EQ_0. Another interesting feature of Fig. 6(b) is that DC_2 initially forms a flat strip bounded by manifold trajectories $\mathbf{u}(\theta_3, t)$ and $\mathbf{u}(\theta_4, t)$ (black curves). However, farther away from EQ_2, this strip widens and folds such that $\mathbf{u}(\theta_3, t)$ and $\mathbf{u}(\theta_4, t)$ come close to each other, trace loops which are strikingly similar in shape, and eventually merge (see inset in Fig. 8). This is not an artifact of low-dimensional projection of the state space. As we explain in the following section, the black trajectories in Fig. 6(b) correspond to heteroclinic connections from EQ_2 to a different ECS (PO_1).

Unlike DC_1 and DC_2, the trajectory $\mathbf{u}(\theta_5, t)$ approaches the solution EQ_1, which has one unstable direction (cf. Table I). Since the stable and unstable manifolds of EQ_1 guide the evolution of trajectories in its neighborhood, we explored their geometry to compute the connection from EQ_2 to EQ_1. Trajectories $\mathbf{u}(\theta, t)$ for $\theta \approx \theta_5$ that approach EQ_1 should subsequently depart following its unstable manifold, which coincides with a pair of trajectories,

$$\mathbf{u}^{\pm}(t) = \mathbf{u}_{eq} \pm \epsilon e^{\lambda_1 t}\, \hat{\mathbf{e}}_1, \tag{7}$$

in the linear neighborhood of EQ_1 (cf. Fig. 1). Here $\hat{\mathbf{e}}_1$ is the unstable eigenvector of EQ_1 and $\epsilon > 0$ is some small constant. In particular, we found a pair of adjacent trajectories $\mathbf{u}(\theta, t)$ and $\mathbf{u}(\theta + \Delta\theta, t)$ with $\theta \approx \theta_5$ approach EQ_1 and depart its neighborhood in opposite directions shadowing $\mathbf{u}^+(t)$ and $\mathbf{u}^-(t)$, respectively. Hence, a heteroclinic connection DC_3 from EQ_2 to EQ_1 lies between these two trajectories, i.e., in the stable manifold of EQ_1.

The projection of DC_3 (black curve) is shown in Fig. 6(a). It was computed by refining the estimate for θ_5 to within $\delta\theta = 2^{-12}\Delta\theta$ using bisection [7,12,23]. This refinement reduced the separation between $\mathbf{u}(\theta_5, t)$ and EQ_1 to $D_0 = 0.002$ [cf. Eq. (6)]. Further refinement in θ did not significantly reduce D_0 since numerical noise on $\mathbf{u}(\theta_5, t)$ amplifies rapidly in the direction of unstable eigenvector $\pm\hat{\mathbf{e}}_1$ of EQ_1. This behavior stems from the strong asymmetry in the real parts of unstable ($\lambda_1 = 0.017$) and weakly stable ($\lambda_{2,3} = -0.003 \pm 0.109i$) eigenvalues of EQ_1. Nevertheless, a better accuracy can be achieved by employing multishooting [35] or approximating DC_3 as a piecewise continuous solution [24]. Using the latter technique allowed us to decrease D_0 to less than 10^{-6}. Recall that, Eq. (7) governs the evolution of trajectories in the unstable manifold of EQ_1 only in its linear neighborhood. Farther away, both $\mathbf{u}^{\pm}(t)$ display turbulent evolution for $t \gg 100\tau_c$ and eventually approach EQ_0. Hence these two trajectories define (long) heteroclinic connections (DC_4, DC_5) from EQ_1 to EQ_0.

B. Dynamics near PO_1 and EQ_3

While trajectories $\mathbf{u}(\theta, t)$ for $\theta \in (\theta_3, \theta_4)$ quickly converge to EQ_0, trajectories just outside this interval exhibit qualitatively different dynamics; this can be inferred from s_m changing abruptly at θ_3 and θ_4. This qualitative difference suggests that trajectories $\mathbf{u}(\theta_3, t)$ and $\mathbf{u}(\theta_4, t)$ play the role of separatrices on the unstable manifold of EQ_2 and hence lie in the stable manifold of another ECS. In the case of $\mathbf{u}(\theta_4, t)$, for example, we found this ECS by inspecting the two trajectories $\mathbf{u}(\theta_4^-, t)$ and $\mathbf{u}(\theta_4^+, t)$ obtained as a result of successive bisections; here $\theta_4^{\pm} = \theta_4 \pm \delta\theta$ with $\delta\theta = 2^{-12}\Delta\theta$. The corresponding state space speed plots are shown in Fig. 7, which suggest that $\mathbf{u}(\theta_4^{\pm}, t)$ evolve almost indistinguishably

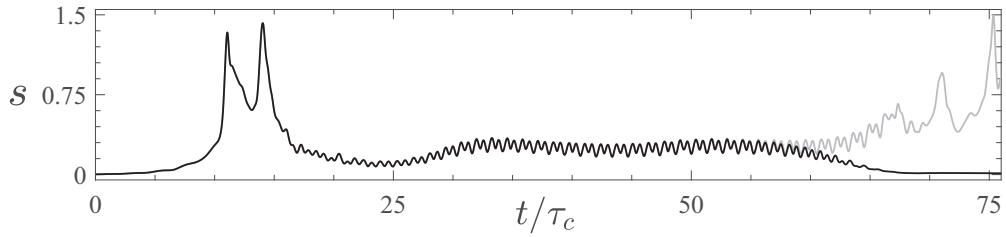

FIG. 7. State space speed along trajectories $\mathbf{u}(\theta_4^-, t)$ (black) and $\mathbf{u}(\theta_4^+, t)$ (gray) that separate after shadowing a periodic orbit.

for about $55\tau_c$ and subsequently separate. For $t/\tau_c \in [30, 55]$ the state space speed oscillates with a period of approximately $1.4\tau_c$, suggesting that $\mathbf{u}(\theta_4^\pm, t)$ shadow a periodic orbit during this interval.

Using the flow field corresponding to $\mathbf{u}(\theta_4^+, t)$ at $t/\tau_c = 55$ as an initial condition into a Newton solver, we indeed found an unstable periodic orbit PO_1 with a period $T = 1.32\tau_c$. A similar refinement using bisection showed that trajectories at $\theta_3^\pm = \theta_3 \pm \delta\theta$ also approach PO_1 and separate after shadowing it for an extended period of time (the corresponding speed plots are not shown). Figure 8 shows the state space projection of $\mathbf{u}(\theta_4^\pm, t)$ and $\mathbf{u}(\theta_3^\pm, t)$ approaching PO_1, shadowing it closely (inset), and subsequently leaving its neighborhood. The projection coordinates here are the same as in Fig. 6, but the viewing angle is different. The result that $\mathbf{u}(\theta_3^\pm, t)$ and $\mathbf{u}(\theta_4^\pm, t)$ approach PO_1 is consistent with the folding of DC_2 shown in Fig. 6(b).

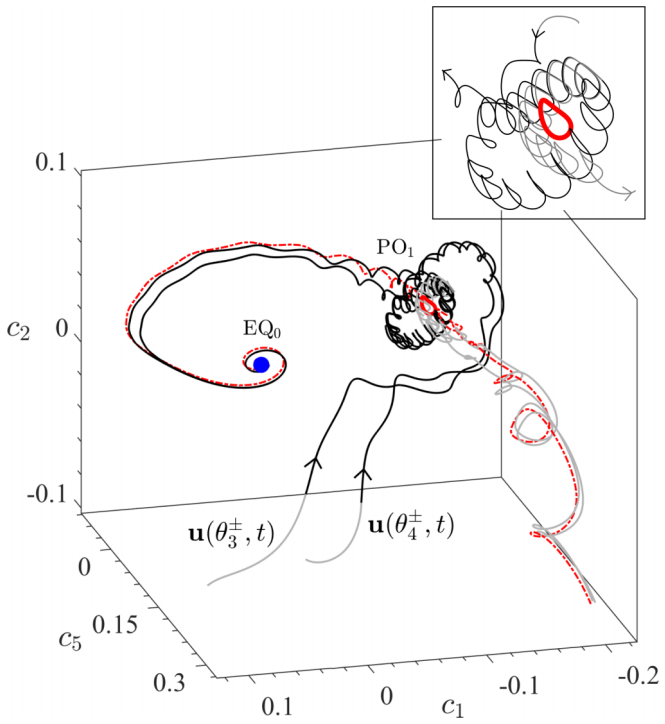

FIG. 8. Geometry of state space around PO_1. Trajectories $\mathbf{u}(\theta_4^\pm, t)$ approach PO_1 indistinguishably but depart from its neighborhood in opposite directions (inset) guided by the manifold trajectories $\mathbf{u}^\pm(\eta, t)$ (dashed red curves). $\mathbf{u}(\theta_4^-, t)$ (black curve) converges to EQ_0 and $\mathbf{u}(\theta_4^+, t)$ (gray curve) becomes turbulent. Similar behavior is manifested by $\mathbf{u}(\theta_3^\mp, t)$.

PO_1 has a single real unstable direction in $\mathcal{S}$ with an associated Floquet exponent $\lambda_1 = 0.036$ (cf. Table I). Hence, the departure of $\mathbf{u}(\theta_3^\pm, t)$ and $\mathbf{u}(\theta_4^\pm, t)$ from the neighborhood of PO_1 is guided by its unstable manifold, which is 2D since it is associated with a PO which is itself one-dimensional (1D). This 2D unstable manifold can be constructed by evolving initial conditions [37],

$$\mathbf{u}^\pm(\eta, 0) = \mathbf{u}_{po} \pm \epsilon e^{\lambda_1 \eta}\, \hat{\mathbf{e}}_1, \tag{8}$$

where $\mathbf{u}_{po}$ is a reference point on PO_1, $\hat{\mathbf{e}}_1$ is the Floquet vector at $\mathbf{u}_{po}$, $\epsilon > 0$ is sufficiently small (we chose $\epsilon = 0.001 \cdot \|\mathbf{u}_{po}\|$), and $\eta \in (0, T]$ parametrizes different initial conditions. A total of 720 initial conditions, equally spaced in η, were generated, and the corresponding trajectories $\mathbf{u}^\pm(\eta, t)$ were computed on an interval of length $35\tau_c$ to approximate the manifold. We found that trajectories $\mathbf{u}^+(\eta, t)$ uneventfully converge to EQ_0 while $\mathbf{u}^-(\eta, t)$ display turbulent evolution after leaving the neighborhood of PO_1. To illustrate this, we plotted in Fig. 8 a pair of trajectories $\mathbf{u}^\pm(\eta, t)$ (red dashed curves) evolving in opposite directions.

Since PO_1 has a single unstable direction, its stable manifold divides the state space in the neighborhood of PO_1 into two halves [54]. We found that trajectories $\mathbf{u}(\theta_3^+, t)$ and $\mathbf{u}(\theta_4^-, t)$ smoothly converge to EQ_0 after approaching PO_1 and hence lie on one (the same) side of the stable manifold. Meanwhile $\mathbf{u}(\theta_3^-, t)$ and $\mathbf{u}(\theta_4^+, t)$ display turbulent excursions and hence lie on the opposite side of the stable manifold, as shown in Fig. 8. Therefore, there exist two heteroclinic connections from EQ_2 to PO_1 sandwiched between $\mathbf{u}(\theta_3^\pm, t)$ (DC_6) and $\mathbf{u}(\theta_4^\pm, t)$ (DC_7), that lie on the stable manifold and asymptotically converge to PO_1. Just like in the case of DC_3, simple shooting cannot be employed to compute DC_6 and DC_7 in their entirety since they are very unstable. Nevertheless, for sufficient refinement in θ, the trajectories $\mathbf{u}(\theta_3^\pm, t)$ and $\mathbf{u}(\theta_4^\pm, t)$ approximate DC_6 and DC_7, respectively, reasonably accurately [cf. Fig. 6(b)]. This was tested by computing the smallest distance between $\mathbf{u}(\theta, t)$ and PO_1,

$$D_1 = \min_{t,\eta} \frac{\|\mathbf{u}(\theta, t) - \mathbf{u}_{po}(\eta)\|}{D_c}, \tag{9}$$

where $\theta = \theta_3^\pm$ or $\theta_4^\pm$ and $\mathbf{u}_{po}(\eta)$ are states along PO_1 parametrized by $\eta \in (0, T]$. We found that $D_1 < 0.005$ in both cases.

Figure 8 shows a toroidal structure traced out by $\mathbf{u}(\theta_4^\pm, t)$ and $\mathbf{u}(\theta_3^\pm, t)$ as these trajectories approach PO_1 along its stable manifold. A magnified view of this region shown in

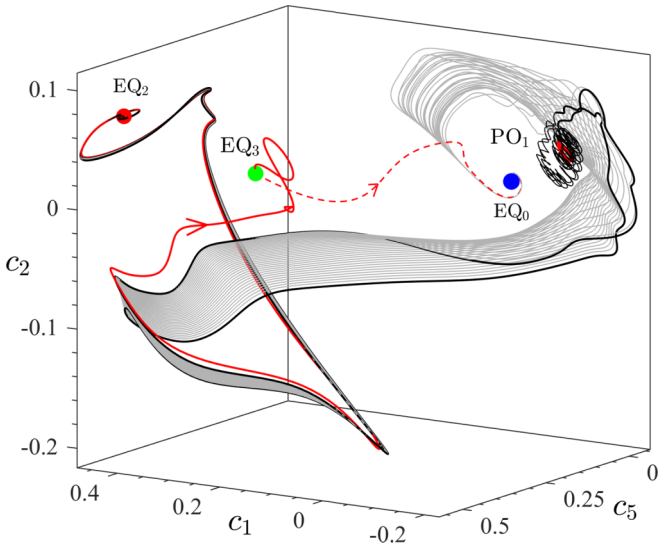

FIG. 9. Heteroclinic connections DC_8, DC_9 (black curves) from EQ_2 to PO_1 that sandwich the family of connections DC_1 (gray curves) from EQ_2 to EQ_0. The solid (dashed) red curve is the connection DC_{10} (DC_{11}) from EQ_2 to EQ_3 (EQ_3 to EQ_0).

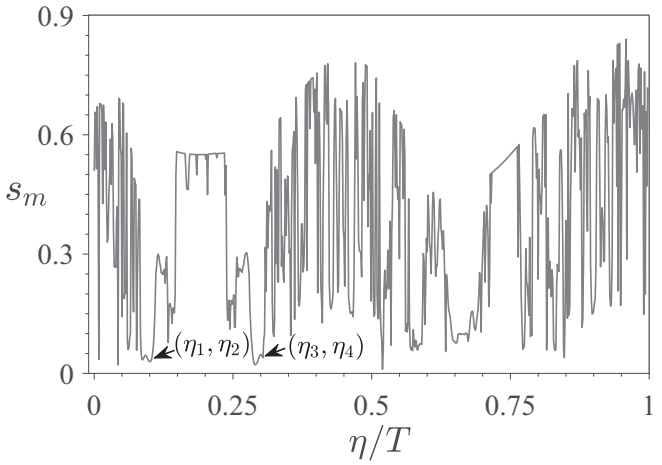

FIG. 10. Minimum state space speed (black curve) s_m along trajectories $\mathbf{u}^-(\eta, t)$ in the 1D unstable manifold of PO_1. $\eta \in [0, T)$ parametrizes points along PO_1.

the inset illustrates the complicated shape of the manifold. The numerous small loops correspond to the fast constant amplitude oscillation along PO_1. In contrast, the large spiral corresponds to a slowly decaying oscillation described by the stable Floquet vectors $\hat{\mathbf{e}}_2$, $\hat{\mathbf{e}}_3$ of PO_1 with exponents $\lambda_{2,3} = -0.0044 \pm 0.0264i$. The characteristic time associated with this slow oscillation is $2\pi/0.0264 \approx 20\tau_c$ and manifests itself in the weak modulation of the state space speed during the interval $t \in [30\tau_c, 50\tau_c]$ in Fig. 7.

As mentioned earlier, based on dimensional arguments, DC_1 should be a 2D manifold which corresponds to a one-parameter family of trajectories connecting EQ_2 to EQ_0. Since the corresponding interval θ_n is very narrow, $\theta_2 - \theta_1 < \Delta\theta$, we resampled a wider interval of width $2\Delta\theta$ that includes θ_n using 100 equally spaced initial conditions. This refinement showed that $\theta_2 - \theta_1 \approx 0.5\Delta\theta$ and all trajectories inside this interval converge to EQ_0, i.e., DC_1 is indeed a 2D manifold. Thirty trajectories from DC_1 are shown (as gray curves) in Fig. 9. The projection coordinates and the viewing angle are the same as in Fig. 6. As in the case of DC_2, the trajectories $\mathbf{u}(\theta_1, t)$ and $\mathbf{u}(\theta_2, t)$ at the left and right edges of DC_1 are separatrices on the 2D unstable manifold of EQ_2. Using bisection, we identified that both $\mathbf{u}(\theta_1, t)$ and $\mathbf{u}(\theta_2, t)$ approach PO_1 closely ($D_1 < 0.005$) and well-approximate heteroclinic connections DC_8, DC_9 from EQ_2 to PO_1 shown (as black curves) in Fig. 9.

The refinement in initial conditions around θ_n also revealed that a few trajectories $\mathbf{u}(\theta, t)$ for $\theta_1 - \Delta\theta < \theta < \theta_1$ approach an unstable equilibrium EQ_3. The flow field corresponding to EQ_3 is shown in Fig. 2(d). EQ_3 has a single unstable direction in $\mathcal{S}$ and its unstable manifold is one-dimensional, similar to EQ_1 (see Fig. 1). Also, we found that a pair of adjacent trajectories from EQ_2 approach EQ_3 and subsequently depart in opposite directions. Hence, using bisection we computed the heteroclinic connection DC_{10} from EQ_2 to EQ_3 (solid red curve in Fig. 9). Additionally, we also found that one of the manifold trajectories of EQ_3 uneventfully converges to EQ_0. This connection (DC_{11}) is also shown (as dashed red curve) in Fig. 9. The manifold trajectory from EQ_3 evolving in the opposite direction, however, also converged to EQ_0 after a long turbulent excursion and hence corresponds to another connection (DC_{12}). This qualitative difference in dynamics on the two sides of the stable manifold of EQ_3 is not observed in case of EQ_1. As mentioned previously, both trajectories in the 1D unstable manifold of EQ_1 display long turbulent excursions.

C. Connections originating at PO_1

As we have established, all trajectories $\mathbf{u}^+(\eta, t)$ from PO_1 quickly converge to EQ_0 (cf. Fig. 8). These trajectories constitute a one-parameter family of heteroclinic connections from PO_1 to EQ_0 which form a 2D manifold DC_{13}. The union of DC_6 and DC_7 forms a 1D boundary of the union of the 2D manifolds DC_2 and DC_{13}. Similarly, the union of DC_8 and DC_9 forms a 1D boundary of the union of 2D manifolds DC_1 and DC_{13}.

Unlike $\mathbf{u}^+(\eta, t)$, the trajectories $\mathbf{u}^-(\eta, t)$ display turbulent excursions after departing from the neighborhood of PO_1. Hence, we tested whether for some η they approach other ECSs, as in the case of trajectories $\mathbf{u}(\theta, t)$ in the 2D unstable manifold of EQ_2 (cf. Sec. III A). Since $\mathbf{u}^-(\eta, t)$ is also a one-parameter family of trajectories, we followed the procedure discussed in Sec. III A to search for signatures of dynamical connections originating at PO_1.

To begin, we computed the state space speed $s(\eta, t)$ for each trajectory $\mathbf{u}^-(\eta, t)$ (e.g., Fig. 16 in Appendix B) and calculated $s_m(\eta) = \min_t s(\eta, t)$ for $t/\tau_c \in [15, 35]$. From the plot of s_m versus η, shown in Fig. 10, we identified about 20 trajectories with $s_m \ll 1$ as possible dynamical connections. Surprisingly, *all* these trajectories converged to EQ_0. This was tested by extending the corresponding $\mathbf{u}^-(\eta, t)$ until the separation from EQ_0 decreased to $D_0 < 0.01$. Since a detailed analysis of dynamics along all of these trajectories is not feasible, we limit the discussion to the families of

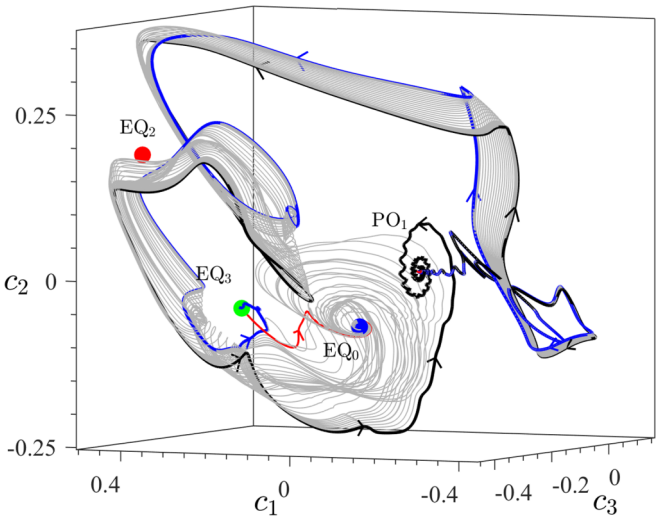

FIG. 11. Family of heteroclinic connections (DC_{14}, gray curves) from PO_1 to EQ_0. The black curve is a homoclinic orbit of PO_1 (DC_{15}) and the blue curve is a heterodinic connection from PO_1 to EQ_3 (DC_{16}). The red curve is DC_{11} from EQ_3 to EQ_0.

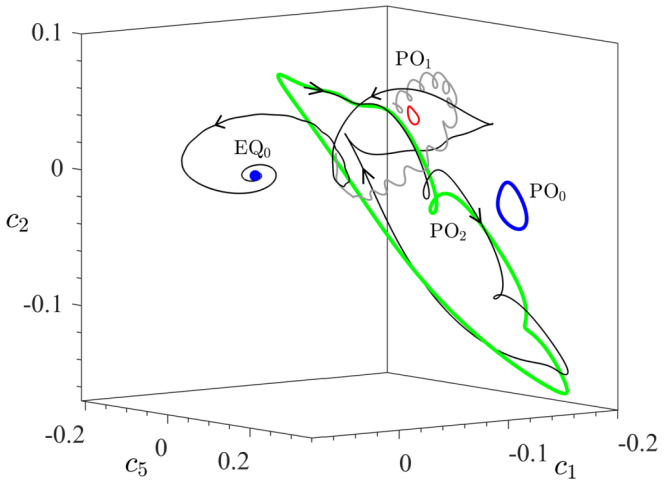

FIG. 12. Heteroclinic connections from PO_2 (green loop) to EQ_0 (DC_{20}, black curve) and PO_1 (DC_{21}, gray curve). DC_{21} eventually converges to PO_1 tracing out a helical path similar to that shown in Fig. 8.

connections DC_{14} that correspond to the interval (η_1, η_2) marked in Fig. 10.

About 30 trajectories (gray curves) from the family DC_{14} are shown in Fig. 11, which, unlike all other figures, employs a projection of the state space onto an orthonormal basis constructed from Floquet vectors $\hat{\mathbf{e}}_1$ (unstable, real) and $\hat{\mathbf{e}}_2$, $\hat{\mathbf{e}}_3$ (stable, complex conjugate pair) of PO_1. Trajectories in DC_{14} leave the neighborhood of PO_1 along $\hat{\mathbf{e}}_1$. After a brief turbulent excursion, they visit the neighborhood of EQ_2 and finally converge to EQ_0. An interesting feature of Fig. 11 is that several trajectories in DC_{14} appear to visit the neighborhood of PO_1 *en route* to EQ_0. This raises the question of whether a homoclinic orbit $\mathbf{u}^-(\eta, t)$ of PO_1 exists near the interval (η_1, η_2). Since PO_1 has one unstable direction, a homoclinic orbit should be sandwiched between trajectories that show qualitatively different dynamics [39]. Such a behavior is indeed observed for trajectories near η_1 and η_2 where s_m changes abruptly. Using bisection, we refined the estimate for η_2 and found that $\mathbf{u}^-(\eta_2, t)$ indeed approaches PO_1 very closely (within $D_1 < 0.005$) and therefore well-approximates a homoclinic connection DC_{15} shown (black curve) in Fig. 11. The projection used in this figure allows visualization of the asymptotic dynamics along DC_{15} for both early times (on the unstable manifold of PO_1) and late times (on the stable manifold of PO_1). Refining the estimate for η_1 using bisection revealed that $\mathbf{u}^-(\eta_1, t)$ instead converges to EQ_3 (with $D_0 = 5\times10^{-4}$), approximating a heteroclinic connection DC_{16} (blue curve in Fig. 11).

We found that trajectories $\mathbf{u}^-(\eta, t)$ in the interval marked (η_3, η_4) in Fig. 10 also converge to EQ_0, after a brief turbulent excursion. These trajectories constitute a one-parameter family of connections DC_{17} from PO_1 to EQ_0. Using bisection, we identified that $\mathbf{u}^-(\eta_3, t)$ is another homoclinic orbit (DC_{18}) of PO_1 while $\mathbf{u}^-(\eta_4, t)$ is a heteroclinic connection (DC_{19}) from PO_1 to EQ_3. The shapes of DC_{17}, DC_{18}, and DC_{19} are very similar to that of DC_{14}, DC_{16}, and DC_{15}, respectively, and hence are not shown. Note that we have so far inspected state space along manifold trajectories to detect signatures of dynamical connections to EQs. An alternative metric, which allows one to identify signatures of close passes to both EQs and POs, is discussed in more detail in Appendix B. Trajectories $\mathbf{u}^-(\eta, t)$ originating at PO_1 are analyzed using both metrics, and the results are compared in Fig. 16 below.

D. Connections originating at PO_2

Visual inspection of state space speed and recurrence plots (e.g., Fig. 16 below) revealed that some turbulent trajectories $\mathbf{u}^-(\eta, t)$ from PO_1 shadow an unstable periodic orbit PO_2. This orbit, which we computed using a Newton solver, has a period $T = 4.61\tau_c$ and is only moderately repelling in $\mathcal{S}$; its leading Floquet exponents are $\lambda_1 = 0.044$, $\lambda_{2,3} = -0.019 \pm 0.016i$. However, we did not find evidence of a short heteroclinic connection from PO_1 to PO_2, i.e., $\mathbf{u}^-(\eta, t)$ for $t/\tau_c \in (15, 35)$ did not approach PO_2 very closely. Hence, we tested whether a connection instead exists from PO_2 to PO_1.

The 2D unstable manifold of PO_2 is composed of two sets of trajectories $\mathbf{u}^{\pm}(\xi, t)$ that start from initial conditions $\mathbf{u}^{\pm}(\xi, 0)$ constructed using Eq. (8). Here ξ (instead of η) parametrizes states along PO_2 as well as the trajectories $\mathbf{u}^{\pm}(\xi, t)$. Unlike the unstable manifold of PO_1, we found that trajectories in both $\mathbf{u}^+(\xi, t)$ and $\mathbf{u}^-(\xi, t)$ display turbulent evolution. Hence, we analyzed $\mathbf{u}^-(\xi, t)$ as well as $\mathbf{u}^+(\xi, t)$ for signatures of dynamical connections; the plot of $s_m(\xi)$ for each set is included as Fig. S1 in the Supplemental Material [8]. Inspecting state space speed (as well as recurrence) plots for each trajectory and following the procedure outlined in the previous sections, we identified a family of heteroclinic connections from PO_2 to EQ_0 (DC_{20}) and two isolated connections to PO_1 (DC_{21}, DC_{22}) that lie at the boundary of DC_{20}. A connection from the family DC_{20} (black curve) and the isolated connection DC_{21} (gray curve) are shown in Fig. 12. The projection coordinates here are the same as in Fig. 8, and the viewing angle is similar. We note that DC_{20}, DC_{21},

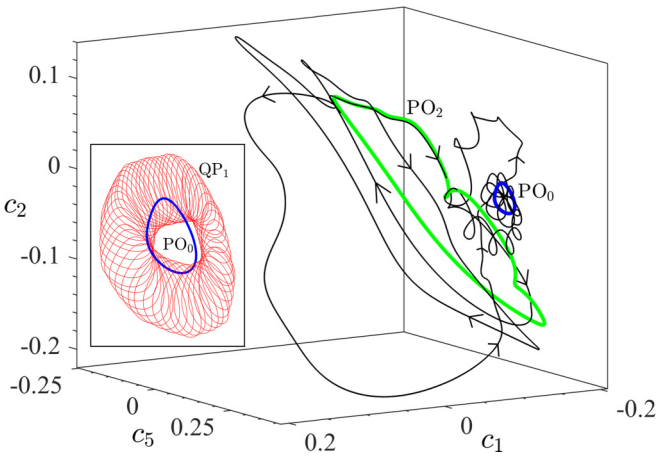

FIG. 13. Heteroclinic connection DC_{23} from PO_2 (green loop) to PO_0 (blue loop). The inset shows the unstable quasiperiodic orbit QP_1 (red curve) that lies near stable PO_0.

and DC_{22} (not shown) approach their respective destinations quickly after leaving the neighborhood of PO_2.

We also found that a narrow band of trajectories $\mathbf{u}^+(\xi,t)$ for $\xi \in (\xi_1,\xi_2)$ from PO_2 approach a periodic orbit PO_0 shown in Fig. 12. PO_0 has a period $T = 1.22\tau_c$ and is stable in $\mathcal{S}$, with its leading Floquet exponent being $\lambda_{1,2} = -0.0026 \pm 0.059i$. Hence, a one-parameter family of connections DC_{23} from PO_2 to PO_0 was computed by evolving $\mathbf{u}^+(\xi,t)$ for $\xi \in (\xi_1,\xi_2)$ for $t \approx 400\tau_c$. The state space projection of a trajectory from the family DC_{23} is shown in Fig. 13. Since PO_0 is stable in $\mathcal{S}$, DC_{23} is a 2D manifold and trajectories that correspond to the left (ξ_1) and right (ξ_2) edges separate trajectories converging to PO_0 from those which become turbulent. Using bisection, we found that both $\mathbf{u}^+(\xi_1,t)$, $\mathbf{u}^+(\xi_2,t)$ approach a 2-torus representing an unstable quasiperiodic orbit (QPO) QP_1 shown in Fig. 13 (inset). Hence, $\mathbf{u}^+(\xi_1,t)$, $\mathbf{u}^+(\xi_2,t)$ correspond to connections DC_{24}, DC_{25} from PO_2 to QP_1.

The state space speed for $\mathbf{u}^+(\xi_1,t)$ clearly shows dynamics with two different frequencies over a time interval $70\tau_c$ (Fig. S2 in the Supplemental Material) [8]. Computing recurrence plots for this segment of $\mathbf{u}^+(\xi_1,t)$, we estimated that the periods associated with large and small loops of QP_1 are $T_1/\tau_c = 12.21 \pm 0.018$ and $T_2/\tau_c = 1.21 \pm 0.05$, respectively. Since the ratio $T_1/T_2 \approx 10.05$ is close to an integer, we also used the Newton-Krylov solver to test whether QP_1 is instead a periodic orbit with period $T \approx T_1$, $2T_1$, or $3T_1$; in all cases the solver failed to converge, suggesting that QP_1 is indeed a QPO. The procedure we used to compute QP_1 also suggests that this solution (just like PO_1) possesses just one unstable direction in $\mathcal{S}$ and its stable manifold separates initial conditions that quickly approach PO_0 from those exhibiting transient turbulence. Computing the stability exponents of QP_1, however, is beyond the scope of this study. Trajectories from QP_1 that uneventfully converge to PO_0 constitute a two-parameter family of connections forming a 3D manifold (DC_{26}).

E. Structural stability of dynamical connections

All dynamical connections we reported so far were computed at $\mathrm{Re} = 22.05$. One may ask if these connections are robust to small changes in Re, i.e., whether these connections are structurally stable [33]. Recall that a connection from $ECS_{-\infty}$ to ECS_{∞} is formed by an intersection of the unstable manifold of $ECS_{-\infty}$ and the stable manifold of ECS_{∞}, with respective dimensions $d_u^{-\infty}$ and d_s^{∞}. If these two manifolds intersect (in our case we have shown that they do), their intersection will generically be of dimension $d = d_u^{-\infty} + d_s^{\infty} - N$, where N is the dimension of the state space (in our case $\mathcal{S}$). We should have $d > 0$ for the connection to be structurally stable.

TABLE II. Dynamical connections computed at $\mathrm{Re} = 22.05$.

	$ECS_{-\infty}$	ECS_{∞}	d	$d_u^{-\infty}$	k_s^{∞}
DC_1, DC_2	EQ_2	EQ_0	2	2	0
DC_3	EQ_2	EQ_1	1	2	1
DC_4, DC_5	EQ_1	EQ_0	1	1	0
DC_6–DC_9	EQ_2	PO_1	1	2	1
DC_{10}	EQ_2	EQ_3	1	2	1
DC_{11}, DC_{12}	EQ_3	EQ_0	1	1	0
DC_{13}, DC_{14}, DC_{17}	PO_1	EQ_0	2	2	0
DC_{15}, DC_{18}	PO_1	PO_1	1	2	1
DC_{16}, DC_{19}	PO_1	EQ_3	1	2	1
DC_{20}	PO_2	EQ_0	2	2	0
DC_{21}, DC_{22}	PO_2	PO_1	1	2	1
DC_{23}	PO_2	PO_0	2	2	0
DC_{24}, DC_{25}	PO_2	QP_1	1	2	1
DC_{26}	QP_1	PO_0	3	3	0

Since both d_s^{∞} and N are typically very large (or infinite), d can be expressed in a more convenient form in terms of the codimension $k_s^{\infty} = N - d_s^{\infty}$ of the stable manifold of ECS_{∞} [12]. If N_u^{∞}, N_s^{∞}, and N_m^{∞} are the number of unstable, stable, and marginal directions of ECS_{∞}, then $N_u^{\infty} + N_s^{\infty} + N_m^{\infty} = N$ and $d_s^{\infty} = N_s^{\infty} + N_m^{\infty}$. Hence, $k_s^{\infty} = N_u^{\infty}$ which yields $d = d_u^{-\infty} - N_u^{\infty}$. The criterion ($d > 0$) for the structural stability of a connection is then simply $d_u^{-\infty} > N_u^{\infty}$. Table II lists the various connections we computed and the corresponding dimensions for each connection. The entire network of connections is also shown in schematic form in Fig. 14. Clearly, all of our connections satisfy the structural stability criterion.

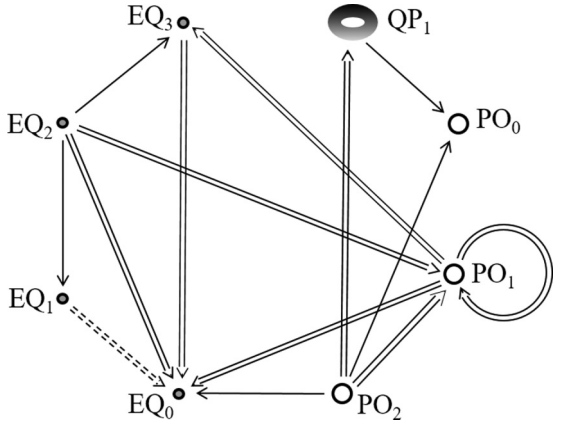

FIG. 14. Topology of connections. Double lines represent multiple distinct connections. Solid (dashed) lines represent short (long) connections.

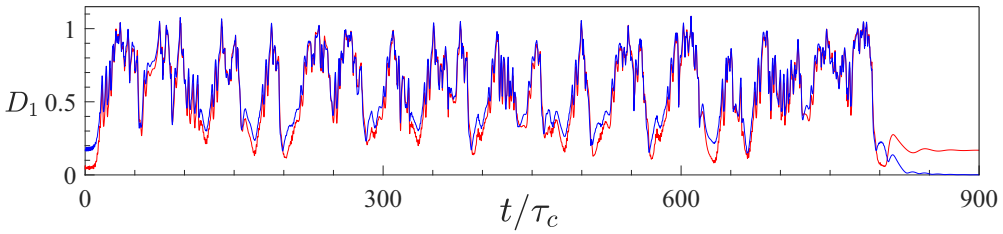

FIG. 15. Instantaneous distances from a long transient turbulent trajectory to PO_1 (D_1, red) and EQ_0 (D_0, blue). Repeated close passes to PO_1 suggest that the homoclinic tangle between the stable and unstable manifolds of PO_1 underpins transient turbulence in symmetric subspace. Vanishing of D_0 implies convergence to EQ_0.

We also numerically validated the structural stability of the connections computed at $\mathrm{Re} = 22.05$ by continuing the ECSs for $\mathrm{Re} \in [21.85, 22.2]$ and analyzing their unstable manifolds. For $\mathrm{Re} \in [21.85, 22.2]$ the number of unstable directions of all the ECSs we computed (except PO_2) remained unchanged. PO_2 exists only for $\mathrm{Re} \geqslant 22.0$, and its unstable manifold was analyzed only at $\mathrm{Re} = 22.2$.

F. Transient turbulence

As we discussed previously, turbulence in the symmetry subspace $\mathcal{S}$ is transient, with most initial conditions eventually "relaminarizing" by converging to the stable equilibrium EQ_0. While some states relaminarize relatively quickly, others stay turbulent for a significant interval of time. It is natural to ask what geometric structures are responsible for maintaining turbulent flow and for relaminarization. Our results show that the periodic orbit PO_1 plays a key role in both processes. As we have demonstrated, PO_1 possesses (at least) two distinct homoclinic connections (DC_{15}, DC_{18}). The presence of homoclinic connections, which lie at the intersection of the stable and unstable manifold of PO_1, suggests that these manifolds intersect and form a homoclinic tangle. The tangle explains the fractal nature of the minimal state space speed shown in Fig. 10, which results from stretching and folding of the unstable manifold. More importantly, it implies the presence of a chaotic set (a chaotic repeller in our case) anchored by PO_1 as well as the presence of arbitrarily long periodic orbits that visit the neighborhood of PO_1 [33]. These are precisely the ingredients required for transient turbulence.

To show that it is indeed the homoclinic tangle associated with PO_1 that underlies transient turbulence in our system, we computed the distance D_1 (D_0) from PO_1 (EQ_0) to a particular long turbulent trajectory. As Fig. 15 demonstrates, the trajectory returns to the vicinity of PO_1 many times before finally relaminarizing i.e., converging to EQ_0 ($D_0 \to 0$). Furthermore, just before relaminarization, this trajectory comes very close to PO_1, which suggests PO_1 plays an important role in this process. It should be pointed out that not all trajectories approach PO_1 closely just before relaminarization. Some trajectories pass through the neighborhood of EQ_3 instead, as Fig. 11 illustrates. Both PO_1 and EQ_3 have stable manifolds with codimension one; states on one side of these manifolds relaminarize almost immediately, and those on the other side exhibit transient turbulence. Hence, these two stable manifolds form portions of a local boundary between "laminar" and "turbulent" flows. This analogy, however, is not perfect since the chaotic set underlying the turbulent transient is not an attractor.

It should be mentioned that nonuniqueness of edge states lying on a "laminar-turbulent" boundary has been previously reported for other turbulent flows as well. For instance, Kerswell [14] and Duguet *et al.* [28] have identified several edge states corresponding to different traveling wave solutions in a short periodic pipe. Our results provide further evidence that not only can multiple edge states coexist, they can be of different types (e.g., an EQ and a PO, in our case).

The relationship between transient turbulence and chaotic repellers has been suggested previously, mainly based on indirect evidence—the power law decay of the relaminarization times characterizing a memoryless process [55–58]. Direct evidence, such as the presence of homoclinic tangles [34,39] or a period-doubling cascade [59], is more recent. Moreover, while the dynamics and stability in systems with heteroclinic cycles have been explored previously [60,61], there is currently very little understanding of dynamics in the presence of both heteroclinic and homoclinic connections. Due to the relative simplicity of the numerical model and ease of experimental access, the system considered here is particularly attractive for studying the relation between transient dynamics, relaminarization, and the structure of connections.

IV. SUMMARY AND CONCLUSIONS

Several recent studies on a dynamical description of fluid turbulence focused on ECSs and how they shape the state space geometry in their neighborhoods. However, complete understanding of turbulence requires a global picture which explains how the flow moves between neighborhoods of ECSs. Such a picture can be considered as a coarse description of the dynamics, in the spirit of symbolic dynamics, analogous to a route network where ECSs serve as nodes and dynamical (heteroclinic and homoclinic) connections as links connecting the nodes. This study is a rigorous attempt to construct such a network for a turbulent fluid flow. We identified eight nodes and several tens of connections between them, far more than any study to date. Moreover, while most previous studies computed connections between ECSs of the same type (primarily EQs), we have identified connections between three different types of ECSs: EQ, PO, and QPO. We have also demonstrated the existence of higher (two- and three-) dimensional connections between ECSs, i.e., continua of trajectories from one ECS to another.

Despite the limited attention they have received, dynamical connections can play a very important role in turbulent evolution [7]. For instance, dynamically dominant ECSs in the Kolmogorov-like flow are equilibria [11]. Being fixed points in the state space, EQs cannot guide turbulent trajectories in their neighborhoods in the same way POs or QPOs do. Therefore, connections between EQs (as well as other types of ECSs) become the dynamically dominant solutions that guide turbulent trajectories, shaping their evolution locally. Even in systems where the dominant solutions are POs or QPOs, ECSs constrain the dynamics only locally in state space and over short intervals of time. The network of connections, on the other hand, constrains the dynamics globally in state space and over arbitrarily long time intervals.

Identifying the connection network has potential applications such as forecasting [5] and control of turbulent flows [62,63]. Even though quantitative prediction has a time horizon set by the leading Lyapunov exponents that characterize the sensitivity to initial conditions, qualitative predictions do not have this limitation. In principle, prediction of extreme events can be made based on the connectivity of different ECSs. Identifying the connection network can also facilitate "low-energy" control of turbulent flows, where small perturbations to the flow result in its subsequent (natural) evolution towards a particular ECS or region of state space with desired behavior [64]. Connections can also provide new insight into laminar-turbulent transition in wall-bounded 3D shear flows [32,39].

In this study, constraining the dynamics to a symmetry invariant subspace lowered the dimensionality of unstable manifolds and dramatically simplified the procedure of computing connections between ECSs. Whether these connections are dynamically relevant in the full state space requires further exploration. Currently, we are lacking robust numerical methods for computing connections between ECSs with more than one or two unstable directions. Some approaches, such as adjoint looping, have shown promise [13], but whether they present a viable option for computing connections between different types of ECSs remains an open problem.

ACKNOWLEDGMENTS

B.S. thanks Burak Budanur for useful discussions and Björn Hof for providing financial support over the duration of this study. The research leading to these results has received funding from the People Programme (Marie Curie Actions) of the European Union's Seventh Framework Programme FP7/2007-2013/ under REA Grant Agreement No. 291734. M.F.S. and R.O.G. acknowledge funding from the National Science Foundation (CMMI-1234436, DMS-1125302, and CMMI-1725587) and Defense Advanced Research Projects Agency (HR0011-16-2-0033).

APPENDIX A: STATE SPACE PROJECTIONS

In this Appendix we briefly describe the procedure used to project the state space onto a low-dimensional subspace spanned by the eigenvectors (Floquet vectors) $\hat{\mathbf{e}}_i$ of an equilibrium (periodic orbit). Each trajectory $\mathbf{u}(t)$ is expressed as a linear combination of the vectors $\hat{\mathbf{e}}_i$ as follows:

$$\mathbf{u}(t) = \mathbf{u}_{\text{ecs}} + \sum_i a_i(t)\,\hat{\mathbf{e}}_i. \tag{A1}$$

Here $\mathbf{u}_{\text{ecs}}$ corresponds to an equilibrium (e.g., EQ_0) or a point on a periodic orbit (e.g., PO_1). The coefficients $a_i(t)$ are computed using the scalar product

$$a_i(t) = \hat{\mathbf{e}}_i^{\dagger} \cdot [\mathbf{u}(t) - \mathbf{u}_{\text{ecs}}], \tag{A2}$$

where $\hat{\mathbf{e}}_i^{\dagger}$ is the adjoint eigenvector (Floquet vector) such that $\hat{\mathbf{e}}_i^{\dagger} \cdot \hat{\mathbf{e}}_j = \delta_{ij}$ (Kronecker delta). Typically, the vectors $\hat{\mathbf{e}}_i$ are not orthonormal ($\hat{\mathbf{e}}_i \cdot \hat{\mathbf{e}}_j \neq \delta_{ij}$). Hence, we construct orthonormalized vectors $\hat{\mathbf{e}}'_j$ such that

$$\hat{\mathbf{e}}_i = \sum_j T_{ij}\,\hat{\mathbf{e}}'_j, \tag{A3}$$

where the matrix elements $T_{ij} = \hat{\mathbf{e}}_i \cdot \hat{\mathbf{e}}'_j$ can be computed using the orthonormality condition $\hat{\mathbf{e}}'_i \cdot \hat{\mathbf{e}}'_j = \delta_{ij}$. The normalized components

$$c_j = \sum_i a_i T_{ij}/D_c \tag{A4}$$

along vectors $\hat{\mathbf{e}}'_i$ are plotted to generate state space projections. Here D_c is the empirically estimated largest separation between two states on a long turbulent trajectory (cf. Sec. III A).

APPENDIX B: RECURRENCE ANALYSIS

In Secs. III A–III D we identified close passes to EQs by computing state space speed $s(t)$ along turbulent trajectories (cf. Fig. 4). However, $s(t)$ is not zero (or constant) for POs, so detecting close passes to POs requires visual inspection of speed plots to find intervals of oscillatory behavior. To address this shortcoming, we tested recurrence analysis [65] in a form similar to that discussed in Duguet *et al.* [9]. For each trajectory $\mathbf{u}(t)$ we computed the normalized recurrence function

$$r(t) = \min_{\tau \in [\tau_l, \tau_h]} \frac{\|\mathbf{u}(t) - \mathbf{u}(t+\tau)\|}{D_c}, \tag{B1}$$

where $0 < \tau_l < \tau_h$ are appropriately chosen constants. Low values of r indicate that the flow field at an instant t nearly recurs during a later interval $[t+\tau_l, t+\tau_h]$. Unlike state space speed, $r(t) = 0$ for $\mathbf{u}(t)$ representing *both* EQs and POs. In the former case τ_l and τ_h are arbitrary, while in the latter case the period T of the orbit should lie inside the interval $[\tau_l, \tau_h]$.

Since a turbulent trajectory shadowing an ECS mimics its spatiotemporal behavior, intervals where $r(t) \ll 1$ correspond to the trajectory visiting neighborhoods of EQs or POs. To identify such visits, however, we should restrict how near (or far) into the future we search for recurrence. Choosing τ_l far smaller than the correlation time τ_c leads to spurious self-recurrence since $\mathbf{u}(t)$ and $\mathbf{u}(t+\tau)$ do not differ appreciably, the extreme case being $r(t) = 0$ when $\tau_l = 0$. The upper bound τ_h restricts the search to short periodic orbits (which

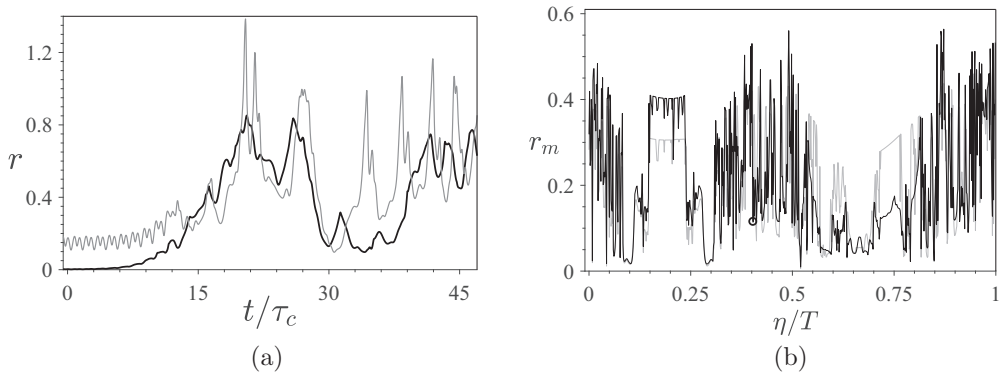

FIG. 16. Recurrence analysis to detect signatures of both EQs and POs (a) Recurrence (black curve) and speed (gray curve) plots for a trajectory that originates at PO_1 and visits the neighborhoods of EQ_0 ($t/\tau_c = 30$) and PO_2 ($t/\tau_c \in [33, 40]$). (b) Minimum recurrence r_m (black curve) and minimum speed s_m (gray curve) for each trajectory $\mathbf{u}^-(\eta, t)$ from PO_1. Trajectories with $r_m \ll 1$ ($s_m \ll 1$) correspond to dynamical connections from PO_1 to EQs/POs (EQs). s_m was scaled such that r_m, s_m have the same mean. Black circle indicates r_m for the trajectory shown in panel (a).

tend to be dynamically relevant [29]) with period $T < \tau_h$. Besides, it also limits the overhead associated with computing $r(t)$. In our analysis we chose $\tau_l = \tau_c$ and $\tau_h = 5\tau_c$.

Figure 16(a) shows recurrence (black curve) and speed (gray curve) plots for a turbulent trajectory $\mathbf{u}(t)$ that originates at PO_1. Initially, $\mathbf{u}(t)$ shadows PO_1 and consequently $s(t)$ displays steady oscillations about a finite value; in contrast, $r(t)$ almost vanishes. After a brief turbulent excursion characterized by r increasing to $O(1)$, $\mathbf{u}(t)$ visits the neighborhoods of EQ_0 at $t/\tau_c \approx 30$ and PO_2 for $33 \lesssim t/\tau_c \lesssim 40$. Both these close passes correspond to r decreasing to well below unity. Hence, to identify signatures of dynamical connections from PO_1 to both EQs and POs, we computed $r(\eta, t)$ for each $\mathbf{u}^-(\eta, t)$ in the unstable manifold of PO_1 (cf. Sec. III B). We then computed $r_m(\eta) = \min_t r(\eta, t)$ for $t > 15\tau_c$, i.e., after each trajectory initially leaves the neighborhood of PO_1. The results are shown in Fig. 16(b), which compares $r_m(\eta)$ (black curve) with $s_m(\eta)$ (gray curve) for each trajectory $\mathbf{u}^-(\eta, t)$. Clearly, the prominent minima of the two metrics align, which suggests that recurrence-based analysis is capable of successfully identifying signatures of close passes to both EQs and POs. However, it is a slightly more expensive method to identify connections, compared with the minimal state space speed.

[1] R. R. Kerswell, Nonlinearity **18**, R17 (2005).
[2] G. Kawahara, M. Uhlmann, and L. van Veen, Annu. Rev. Fluid Mech. **44**, 203 (2012).
[3] B. Hof, C. W. H. van Doorne, J. Westerweel, F. T. M. Nieuwstadt, H. Faisst, B. Eckhardt, H. Wedin, R. R. Kerswell, and F. Waleffe, Science **305**, 1594 (2004).
[4] A. de Lozar, F. Mellibovsky, M. Avila, and B. Hof, Phys. Rev. Lett. **108**, 214502 (2012).
[5] B. Suri, J. Tithof, R. O. Grigoriev, and M. F. Schatz, Phys. Rev. Lett. **118**, 114501 (2017).
[6] E. Hopf, Commun. Pure Appl. Math. **1**, 303 (1948).
[7] J. F. Gibson, J. Halcrow, and P. Cvitanović, J. Fluid Mech. **611**, 107 (2008).
[8] See Supplemental Material at http://link.aps.org/supplemental/10.1103/PhysRevE.100.013112 for (a) videos showcasing side-by-side evolution in state space and physical space for connections DC_1, DC_3, DC_6, DC_{10}, DC_{11}, DC_{13}, DC_{15}, DC_{20}, and DC_{23} and (b) state space speed analysis of trajectories in the unstable manifold of PO_2.
[9] Y. Duguet, A. P. Willis, and R. R. Kerswell, J. Fluid Mech. **613**, 255 (2008).
[10] D. Viswanath and P. Cvitanovic, J. Fluid Mech. **627**, 215 (2009).
[11] B. Suri, J. Tithof, R. O. Grigoriev, and M. F. Schatz, Phys. Rev. E **98**, 023105 (2018).
[12] J. Halcrow, J. F. Gibson, P. Cvitanović, and D. Viswanath, J. Fluid Mech. **621**, 365 (2009).
[13] M. Farano, S. Cherubini, J.-C. Robinet, P. De Palma, and T. M. Schneider, J. Fluid Mech. **858**, R3 (2018).
[14] R. R. Kerswell and O. R. Tutty, J. Fluid Mech. **584**, 69 (2007).
[15] G. Kawahara and S. Kida, J. Fluid Mech. **449**, 291 (2001).
[16] G. Kawahara, Phys. Fluids **17**, 041702 (2005).
[17] D. Viswanath, J. Fluid Mech. **580**, 339 (2007).
[18] J. F. Gibson, J. Halcrow, and P. Cvitanović, J. Fluid Mech. **638**, 243 (2009).
[19] H. Faisst and B. Eckhardt, Phys. Rev. Lett. **91**, 224502 (2003).
[20] H. Wedin and R. Kerswell, J. Fluid Mech. **508**, 333 (2004).
[21] C. C. T. Pringle and R. R. Kerswell, Phys. Rev. Lett. **99**, 074502 (2007).
[22] F. Waleffe, J. Fluid Mech. **435**, 93 (2001).
[23] T. Itano and S. Toh, J. Phys. Soc. Jpn. **70**, 703 (2001).
[24] S. Toh and T. Itano, J. Fluid Mech. **481**, 67 (2003).
[25] J. Kim, P. Moin, and R. Moser, J. Fluid Mech. **177**, 133 (1987).
[26] J. M. Hamilton, J. Kim, and F. Waleffe, J. Fluid Mech. **287**, 317 (1995).
[27] J. Wang, J. Gibson, and F. Waleffe, Phys. Rev. Lett. **98**, 204501 (2007).
[28] Y. Duguet, C. C. T. Pringle, and R. R. Kerswell, Phys. Fluids **20**, 114102 (2008).
[29] P. Cvitanović and J. F. Gibson, Phys. Scr. **2010**, 014007 (2010).

[30] N. B. Budanur, K. Y. Short, M. Farazmand, A. P. Willis, and P. Cvitanović, J. Fluid Mech. **833**, 274 (2017).
[31] G. Lemoult, K. Gumowski, J.-L. Aider, and J. E. Wesfreid, Eur. Phys. J. E **37**, 1 (2014).
[32] N. B. Budanur and B. Hof, J. Fluid Mech. **827**, R1 (2017).
[33] S. Smale, Bull. Amer. Math. Soc. **73**, 747 (1967).
[34] L. van Veen and G. Kawahara, Phys. Rev. Lett. **107**, 114501 (2011).
[35] L. van Veen, G. Kawahara, and M. Atsushi, SIAM J. Sci. Comput. **33**, 25 (2011).
[36] S. Kline, W. Reynolds, F. Schraub, and P. Runstadler, J. Fluid Mech. **30**, 741 (1967).
[37] A. Riols, F. Rincon, C. Cossu, G. Lesur, P.-Y. Longaretti, G. I. Ogilvie, and J. Herault, J. Fluid Mech. **731**, 1 (2013).
[38] A. Pershin, C. Beaume, and S. M. Tobias, J. Fluid Mech. **867**, 414 (2019).
[39] N. B. Budanur, A. S. Dogra, and B. Hof, arXiv:1810.02211.
[40] N. F. Bondarenko, M. Z. Gak, and F. V. Dolzhanskiy, Izv. Akad. Nauk SSSR, Fiz. Atmos. Okeana **15**, 711 (1979).
[41] B. Suri, J. Tithof, R. Mitchell, R. O. Grigoriev, and M. F. Schatz, Phys. Fluids **26**, 053601 (2014).
[42] G. J. Chandler and R. R. Kerswell, J. Fluid Mech. **722**, 554 (2013).
[43] D. Lucas and R. R. Kerswell, J. Fluid Mech. **750**, 518 (2014).
[44] M. Farazmand, J. Fluid Mech. **795**, 278 (2016).
[45] P. Cvitanović, Phys. Rev. Lett. **61**, 2729 (1988).
[46] J. Tithof, B. Suri, R. K. Pallantla, R. O. Grigoriev, and M. F. Schatz, J. Fluid Mech. **828**, 837 (2017).
[47] S. Armfield and R. Street, J. Comput. Phys. **153**, 660 (1999).
[48] B. Suri, Ph.D. thesis, Georgia Institute of Technology, 2017.
[49] J. Farmer, E. Ott, and J. A. Yorke, Physica D **7**, 153 (1983).
[50] S. A. Neelavara, Y. Duguet, and F. Lusseyran, Fluid Dyn. Res. **49**, 035511 (2017).
[51] Y. Saad and M. H. Schultz, SIAM J. Sci. Stat. Comput. **7**, 856 (1986).
[52] C. T. Kelley, *Solving Nonlinear Equations with Newton's Method* (SIAM, Philadelphia, 1995).
[53] R. Mitchell, Ph.D. thesis, Georgia Institute of Technology, 2013.
[54] M. Avila, F. Mellibovsky, N. Roland, and B. Hof, Phys. Rev. Lett. **110**, 224502 (2013).
[55] B. Hof, J. Westerweel, T. M. Schneider, and B. Eckhardt, Nature (London) **443**, 59 (2006).
[56] B. Eckhardt, H. Faisst, A. Schmiegel, and T. M. Schneider, Philos. Trans. R. Soc. London A **366**, 1297 (2007).
[57] T. M. Schneider, F. De Lillo, J. Buehrle, B. Eckhardt, T. Dörnemann, K. Dörnemann, and B. Freisleben, Phys. Rev. E **81**, 015301(R) (2010).
[58] D. Borrero-Echeverry, M. F. Schatz, and R. Tagg, Phys. Rev. E **81**, 025301(R) (2010).
[59] T. Kreilos and B. Eckhardt, Chaos **22**, 047505 (2012).
[60] V. Kirk and M. Silber, Nonlinearity **7**, 1605 (1994).
[61] M. Krupa and I. Melbourne, Ergodic Theory Dyn. Syst. **15**, 121 (1995).
[62] B. Hof, A. de Lozar, M. Avila, X. Tu, and T. M. Schneider, Science **327**, 1491 (2010).
[63] J. Kühnen, B. Song, D. Scarselli, N. B. Budanur, M. Riedl, A. P. Willis, M. Avila, and B. Hof, Nat. Phys. **14**, 386 (2018).
[64] C. C. Pringle, A. P. Willis, and R. R. Kerswell, J. Fluid Mech. **702**, 415 (2012).
[65] J.-P. Eckmann, S. O. Kamphorst, and D. Ruelle, Europhys. Lett. **4**, 973 (1987).